# Perfection of Perovskite Grain Boundary Passivation by Rhodium Incorporation for Efficient and Stable Solar Cells

Wei Liu[1], Nanjing Liu[1], Shilei Ji[1], Hongfeng Hua[1], Yuhui Ma[1], Ruiyuan Hu[1], Jian Zhang[1], Liang Chu[1,3] ✉, Xing'ao Li[1] ✉, Wei Huang[1,2] ✉

✉ Liang Chu, chuliang@njupt.edu.cn; Xing'ao Li, iamxali@njupt.edu.cn; Wei Huang, iamwhuang@njupt.edu.cn

1    Institute of Advanced Materials and New Energy Technology Engineering Laboratory of Jiangsu Province, Nanjing University of Posts and Telecommunications (NUPT), Nanjing 210023, People's Republic of China

2    Shaanxi Institute of Flexible Electronics, Northwestern Polytechnical University, Xi'an 710072, People's Republic of China

3    Guangdong Provincial Key Lab of Nano-Micro Materials Research, School of Chemical Biology and Biotechnology, Peking University Shenzhen Graduate School, Shenzhen 518055, People's Republic of China

## HIGHLIGHTS

- Rhodium ion incorporation helps the nucleation of perovskite grain, passivates the defects in the grain boundaries and enhances the film quality, charge carrier lifetime and mobility.

- After optimizing 1% rhodium into perovskite film, the solar cells achieve an efficiency of 20.71% without obvious hysteresis.

## ABSTRACT

Organic cation and halide anion defects are omnipresent in the perovskite films, which will destroy perovskite electronic structure and downgrade the properties of devices. Defect passivation in halide perovskites is crucial to the application of solar cells. Herein, tiny amounts of trivalent rhodium ion incorporation can help the nucleation of perovskite grain and passivate the defects in the grain boundaries, which can improve efficiency and stability of perovskite solar cells. Through first-principle calculations, rhodium ion incorporation into the perovskite structure can induce ordered arrangement and tune bandgap. In experiment, rhodium ion incorporation with perovskite can contribute to preparing larger crystalline and uniform film, reducing trap-state density and enlarging charge carrier lifetime. After optimizing the content of 1% rhodium, the devices achieved an efficiency up to 20.71% without obvious hysteresis, from 19.09% of that pristine perovskite. In addition, the unencapsulated solar cells maintain 92% of its initial efficiency after 500 h in dry air. This work highlights the advantages of trivalent rhodium ion incorporation in the characteristics of perovskite solar cells, which will promote the future industrial application.



**KEYWORDS** Perovskite solar cells; Grain boundary passivation; Rhodium incorporation
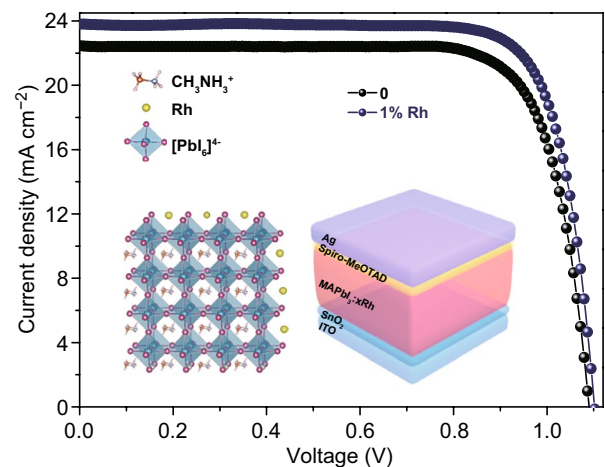
# 1 Introduction

Halide perovskites have attracted great attention owing to the eminent optoelectronic properties, such as suitable energy bandgap [1–6], high absorption coefficient [7–9], long charge diffusion length [10–13] and high carrier mobility [14, 15]. Those advantages boost the improvement in perovskite solar cells (PSCs), being with certified power conversion efficiency (PCE) up to 25.2% [16].

However, pristine perovskite has inevitable internal defects, such as Pb and I vacancy defects, especially in gain boundary, which reduce the performance and stability of PSCs. To date, doping metal ion is an effective strategy to reduce defects, which can improve efficiency and stability of PSCs [17]. For example, doping with monovalent metal cations ($Cu^+$, $Ag^+$ or $Li^+$) was applied to reduce trap-state density [18, 19], improved perovskite crystallinity and film quality, thus enhanced performance of PSCs. By doping bivalent cations ($Mn^{2+}$, $Co^{2+}$ or $Zn^{2+}$), tuned electronic band structures and crystalline morphology were received and improved the stability of PSCs [20–27]. Trivalent metal cations ($In^{3+}$, $Eu^{3+}$ and $Al^{3+}$) were often used to decrease deep defects, optimize film morphology and increase efficiency and stability of PSCs [28–31]. Especially for $Eu^{3+}$ doping, device achieves long-term durability with 92% of the original PCE under continuous illumination for 1500 h [31]. Hence, finding more trivalent metal ions to obtain excellent properties of PSCs is important. The radius of $Rh^{3+}$ is 67 pm, which is less than $Pb^{2+}$ (119 pm). A smaller radius allows both interstitial doping and the possibility of partial replacement of $Pb^{2+}$. Moreover, $4d$ orbital of $Rh^{3+}$ probably tunes electrical properties of perovskite films by heterovalent incorporation [32, 33]. Clearly, compared to elements doped without $d$ orbitals (such as, $Al^{3+}$), such method definitely advances hybrid perovskite materials [30]. Therefore, it is anticipated that $Rh^{3+}$ can be used in hybrid perovskite to enhance the properties of devices.

Here, we utilized $Rh^{3+}$ to be incorporated with $MAPbI_3$ for developing $MAPbI_3$:$xRh^{3+}$ (where $x$ is excessive rhodium mol ratio, and $x = 0$, 0.5, 1.0 and 5.0 mol%). $Rh^{3+}$ incorporation with tiny amounts can help the nucleation of perovskite grain and passivate the defects in perovskite film boundaries. In addition, 1% $Rh^{3+}$ incorporation with perovskite films possesses larger crystalline and less pinhole, which leads to reduce trap-state density and enlarge charge

carrier lifetime. Planar heterojunction PSCs with 1% $Rh^{3+}$ incorporation exhibit high PCE of 20.71% and significantly suppressed photocurrent hysteresis. Compared to other studies of PSCs, the PSCs based on $Rh^{3+}$ incorporation $MAPbI_3$ achieved higher PCE (Table S11). Meanwhile, the devices of 1% $Rh^{3+}$ incorporation have high stability within 500 h without encapsulation in dry air. This work highlights the advantages of $Rh^{3+}$ incorporation in PSCs, which can promote the future industrial application.

# 2 Experimental Section

## 2.1 First-Principle Calculation

All of the density functional theory (DFT) calculations were employed by VASP code [34]. Generalized gradient approximation (GGA) of the projector augmented wave (PAW) was employed [35]. The plane-wave energy cutoff is 500 eV. The energy cutoff convergence is $1 \times 10^{-4}$ eV, and the force cutoff convergence is $-0.09$ eV $Å^{-1}$ [36, 37]. For perovskite structure, $3 \times 3 \times 3$ Monkhorst–Pack grid is taken [38]. The results of calculated lattice constants are well agreed with the experimental from Rietveld refinement (Table S2).

## 2.2 Preparation of Perovskite Single Crystals

For $MAPbI_3$ single crystal, $PbI_2$ (2.835 g) and MAI (0.978 g) were mixed in 5 mL γ-butyrolactone under stirring at 70 °C for 2 h. After heating the solution at 150 °C for 24 h, some obvious single crystals were obtained, which were washed with γ-butyrolactone and dried at 50 °C. Select a relatively large single crystal as the seed crystal, the above reaction was repeated once [11]. For $MAPbI_3$:$xRh$ (where $x = 0.5$, 1 and 5%) single crystal, $x$ is excessive $RhI_3$ incorporation, and the mixed $PbI_2$ and MAI solution was added 0.5, 1 and 5 mol% (0.015, 0.030 and 0.149 g) $RhI_3$, respectively.

## 2.3 Preparation of Devices

$SnO_2$ dense layer (2.67%, diluted by deionized water) was prepared for the cleaned ITO substrate by spin-coated method. For $MAPbI_3$:$xRh$ (where $x = 0$, 0.5, 1, 5%) solution, 159 mg MAI, 470 mg $PbI_2$ and 0, 0.5, 1 and 5 mol %

(0, 2.42, 4.84 and 24.2 mg) $RhI_3$ were separately dissolved in 0.8 mL DMSO:DMF (1:4) solution under room temperature. In total, 35 μL perovskite solution dipped on the $SnO_2$ layers and then spun at 4000 rpm for 20 s. In total, 300 μL chlorobenzene was dipped on the substrate to enhance the film quality when the spinning at 10 s. Then, the substrate was annealed at hot plate. The hole transporting layer Spiro-OMeTAD was spin coated as our previous work [21]. Finally, the PSCs were evaporated 150 nm Ag (0.8 Å s$^{-1}$) with area of 0.09 cm$^2$.

## 3 Results and Discussion

The characteristics of device are closely related to the morphology of the absorption film. Figure 1 shows top-view SEM pictures of MAPbI$_3$:$x$Rh ($x$ = 0, 0.5%, 1% and 5%) ($x$ represents Rh excessive incorporation). At low Rh$^{3+}$-incorporated concentration, such as $x$ = 0.5% and 1%, the grain size becomes larger than pristine MAPbI$_3$ film without Rh$^{3+}$-incorporated (Fig. 1f, g). However, at high Rh$^{3+}$-incorporated concentration (where $x$ = 5%), the quality of film becomes worse (Fig. 1h). The phenomenon was explained both theoretically and experimentally. From the experimental perspective, when the Rh$^{3+}$-incorporated concentration is 0.5% and 1%, a small quantity of Rh$^{3+}$ aggregated near the octahedral [PbI$_6$]$^{4-}$, decreasing the process of perovskite crystallization, organizing large crystalline and uniform perovskite films (Fig. 2a). However, when the Rh$^{3+}$-incorporated concentration is over 5%, on the one hand, a large number of excessive Rh$^{3+}$ aggregate at octahedral [PbI$_6$]$^{4-}$ and prevent the crystallization of perovskite, resulting in the poor-quality film; on the other hand, both Rh$^{3+}$ and Pb$^{2+}$ may be acted as the nuclei to quick crystallization and form discontinuous perovskite films (Fig. 2c) [24]. Thus, when perovskite thin films are based on MAPbI$_3$:$x$Rh (where $x$ = 5%), the film appears pinhole (Fig. 1h). The reason for this change in perovskite films is the different speed of film formation (Fig. 2). From a theoretical point of view, when the Rh$^{3+}$-incorporated concentration of Rh$^{3+}$ is 1%, Rh$^{3+}$ through chemical bonds with the surrounding [PbI$_6$]$^{4-}$ is to induce ordered arrangement and reduce defects [18]. However, when the Rh$^{3+}$-incorporated concentration of Rh$^{3+}$ is up to 5%, partial Rh$^{3+}$ may replace Pb$^{2+}$ to form additional perovskite structures. From intersecting surface SEM

pictures of PSCs fabricated by MAPbI$_3$ and MAPbI$_3$:$x$Rh (where $x$ = 1%), there is no pinhole in the cross section after Rh$^{3+}$ incorporation. This shows that Rh$^{3+}$ incorporation makes both plane and cross section of perovskite continuous [39]. The film thicknesses with its deviations from (where $x$ = 0, 1%) layers are 380 and 400 nm. Electron energy loss spectroscopy (EELS) mapping analysis of MAPbI$_3$:$x$Rh (where $x$ = 1%) shows that the atomic % is also similar to the ratio of experimental preparation (Table S1). From EELS mapping, most of rhodium atoms are distributed at the grain boundary. By grain boundary passivation of rhodium ions, larger perovskite grains without pinholes film were formed (Fig. 1g). In order to explore physical mechanism of MAPbI$_3$:$x$Rh materials, we prepared the MAPbI$_3$:$x$Rh (where $x$ = 0, 0.5%, 1% and 5%) single crystal (Fig. S3). From Fig. 1k, l, XRD was measured to research the crystallinity of MAPbI$_3$:$x$Rh single crystalline. The peaks of 14° and 28° that correspond to the (101) and (202) lattice planes can be clearly seen from XRD, which is indicated that the MAPbI$_3$:$x$Rh possesses excellent crystallinity. No other peaks are observed for the MAPbI$_3$:$x$Rh perovskites, which are indicated that the Rh$^{3+}$ and Pb$^{2+}$ cations have not formed different kinds of phases. Moreover, the diffraction angles are slight lessening when it is 0.5% Rh$^{3+}$ incorporation MAPbI$_3$ (Fig. 1k). The reason of that is the unit cell of MAPbI$_3$:$x$Rh (where $x$ = 0.5%) was enlarging from Rietveld refinement result (Table S2). However, when there is excessive 5% Rh$^{3+}$ incorporation, the peak shift to a higher diffraction angle indicates the lattice parameters decrease. Maybe smaller Rh$^{3+}$ cations partially displace the larger Pb$^{2+}$ cations and the cell volume decreases (Table S2).

We set up the corresponding model and study electronic and optical properties of MAPbI$_3$:$x$Rh (where $x$ = 0, 6%, 8% and 12.5%) and MAPb$_{0.875}$Rh$_{0.125}$I$_3$ (Figs. 2 and S1, S5) based on the result of XRD Rietveld refinement. In perovskite system, iodide ion and methylamine ion are easy to dissociate, which is destroyed perovskite structure and resulted in iodine vacancy defect and methylamine ion vacancy defect. From first-principle calculation, the binding energy (formula as $E = E_{doped} - E_{bulk} - E_{doping\,atom}$) is $-3.45$ eV [40], indicating that Rh$^{3+}$ can easily insert into the interstices of perovskite through the chemical bonds with iodine ion to enhance the stability of perovskite structure and prevent the ions from escaping and reduce iodine vacancy defects. Therefore, the crystallization of perovskite, tiny amount
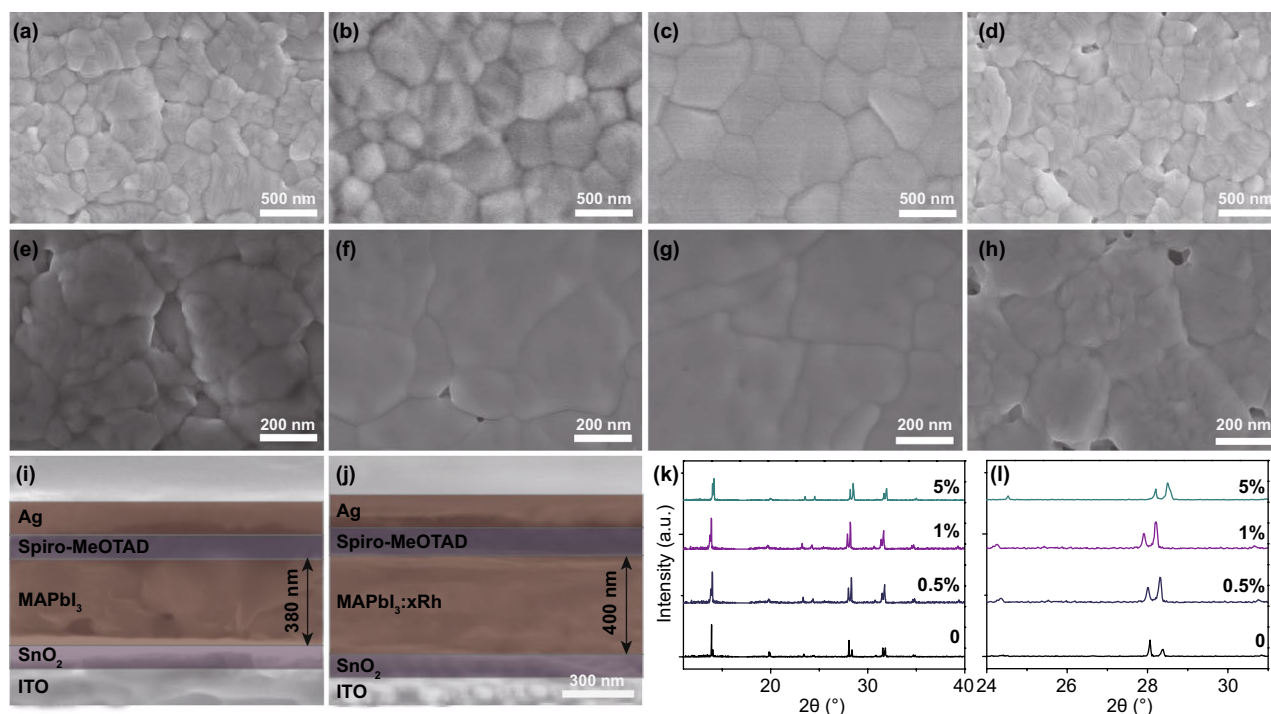
**Fig. 1** SEM pictures of MAPbI$_3$:$x$Rh [where $x=0$ (**a**, **e**), 0.5% (**b**, **f**), 1% (**c**, **g**) and 5% (**d**, **h**)] films. **i**, **j** Cross-sectional pictures of PSCs fabricated by MAPbI$_3$:$x$Rh (where $x=0$, 1%). **k**, **l** XRD patterns of the MAPbI$_3$:$x$Rh single crystal (where $x=0$, 0.5%, 1% and 5%)

of Rh$^{3+}$ is near the octahedral [PbI$_6$]$^{4-}$ to induce ordered arrangement of organic cations to form high-quality film with few defects (Fig. 2a). From first-principle calculation, the bandgap values of MAPbI$_3$:$x$Rh (where $x=0$, 6%, 8% and 12.5%) and MAPb$_{0.875}$Rh$_{0.125}$I$_3$ are 1.31, 1.84, 1.14, 0.80 and 1.15 eV, respectively. The calculated bandgap of 1.31 is similar to experimental bandgap of 1.57 eV. There is a small error in the results of experiment and calculation. For the density of states (DOS) of MAPbI$_3$, valence band maximum (VBM) and conduction band minimum (CBM) are mainly affected by orbitals hybridization of I and Pb. When rhodium ions are interatrial in perovskite structure, hybridization between rhodium and other atomic orbitals affects the distribution of DOS. From Fig. 2a, the rhodium atom makes the conduction band minimum move toward a higher energy level, thus increasing the bandgap. In Fig. 2b, DOS and band structure shows that the MAPbI$_3$ are nonmagnetic. From Fig. 2a, the spin-up and spin-down band structure is not imperfect symmetry, suggesting MAPbI$_3$:$x$Rh possesses magnetism. The calculated total magnetic moment of MAPbI$_3$:$x$Rh (where $x=6$%) atom is 2.254 μB mainly

attributed to Rh atom. This indicates the potential application of this material in the field of magnetism.

XPS was also further to verify Rh$^{3+}$ incorporation and study chemical bonding states of the MAPbI$_3$:$x$Rh structure. Figure 3a shows a separation of approximately 11.6 eV from I 3$d_{3/2}$ and 3$d_{5/2}$ spectra. As the Rh concentration increased, the binding energy (BE) of I 3$d$ is slightly toward higher. From Fig. 3b, the BE of the Pb 4$f_{7/2}$ was about 136.5 eV. As the Rh concentration is increased, the BE of Pb 4$f$ is also slightly toward higher. This small transition to high binding energy may be the shorter Rh–I distance than Pb–I distance, which is lead to higher energy of Pb(Rh)–I bond. We can also observe from the Rietveld refinement above (Table S2). In addition, as the Rh$^{3+}$-incorporated concentration increases, the 1$s$ orbital of N also moves to a higher binding energy. Stronger interactions of Rh–I bond can reduce iodine vacancy defects. The peak at 315 and 308 eV of MAPbI$_3$:$x$Rh (where $x=1$%) film indicates the presence of Rh elements (Fig. 3d).

In order to study the distribution of energy level, absorbance coefficient and ultraviolet photoelectron spectroscopy (UPS) spectra were tested. When the Rh$^{3+}$-incorporated
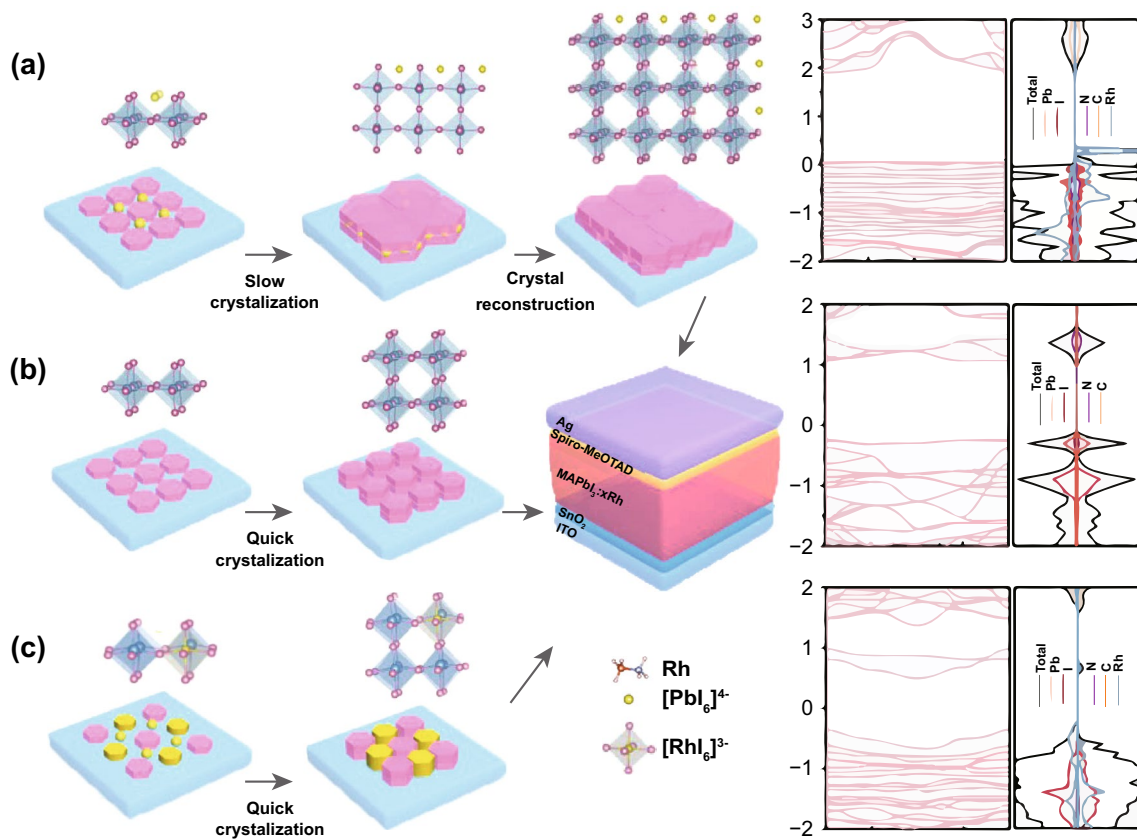
**Fig. 2** Schematic plot of mechanism for $Rh^{3+}$-induced perovskite crystallization. **a** 1% $Rh^{3+}$-incorporated in $MAPbI_3$ through Rh-N band and Rh-I band to form large crystalline structure. **b** Pristine $MAPbI_3$ film formed by quick crystallization. **c** 5% $Rh^{3+}$-incorporated in $MAPbI_3$ film. The diagram on the right is the corresponding band structures and density of states from the first principles (**a** interstitial 6% Rh incorporation, **b** $MAPbI_3$, **c** $MAPb_{0.875}Rh_{0.125}I_3$)

concentration increased from 0 to 1%, the intensity of the absorption spectrum also increased. However, absorption intensity of 5% $Rh^{3+}$ incorporation decreases, which may be related to the quality deterioration of perovskite films. We also calculated the absorption spectra, which were generally consistent with the experiment (Fig. S5a). The bandgap of $MAPbI_3$:$x$Rh is calculated by converting the UV/Vis absorption spectrum into Tauc plots (Fig. 3g). On the basis of the Kubelka–Munk theory [21], the bandgap of $MAPbI_3$:$x$Rh (where $x = 0$, 0.5%, 1% and 5%) is determined to be 1.570, 1.58, 1.58 and 1.59 eV, respectively. From Figs. 3f and S5a, with the increase of $Rh^{3+}$-incorporated concentration, the absorption range was slightly blue shift and basically consistent with the increase of bandgap. Figure 3h shows UPS image of $MAPbI_3$:$x$Rh (where $x = 0$, 0.5%, 1% and 5%). The specific energy levels were calculated from UPS and UV/Vis absorption (Fig. 3i). The formula for calculating the Fermi

energy level is $E_F = 21.22 − E_B$ [21] (where $E_F$ is the Fermi level, and $E_B$ is high binding energy cutoff). The high binding energy cutoff of $MAPbI_3$ is 16.89 eV. $E_F$ of $MAPbI_3$ is $−4.33$ eV (21.22–16.89). The VBM of $MAPbI_3$ is the $E_F$ minus low binding energy as $−5.48$ eV ($−4.33$–1.15). The CBM of $MAPbI_3$ is the sum of VBM and bandgap as $−3.91$ eV. Other detail energy levels of $MAPbI_3$:$x$Rh can be calculated in this way. Energy level diagram of $MAPbI_3$:$x$Rh (where $x = 0$, 0.5%, 1% and 5%) is shown in Fig. 3i. The detailed analysis of energy levels is shown in Table S3.

The current density versus voltage ($J$–$V$) curve is important to study photovoltaic properties. $J$–$V$ curves of PSCs are fabricated by structure of ITO/$SnO_2$/$MAPbI_3$:$x$Rh/Spiro-MeOTAD/Ag (Fig. 4a). Device photovoltaic parameters with $MAPbI_3$:$x$Rh are shown in detail (Table 1). PSCs fabricated by pristine perovskite possess short-circuit current density ($J_{sc}$) of 22.46 mA $cm^{−2}$, open-circuit voltage ($V_{oc}$) of
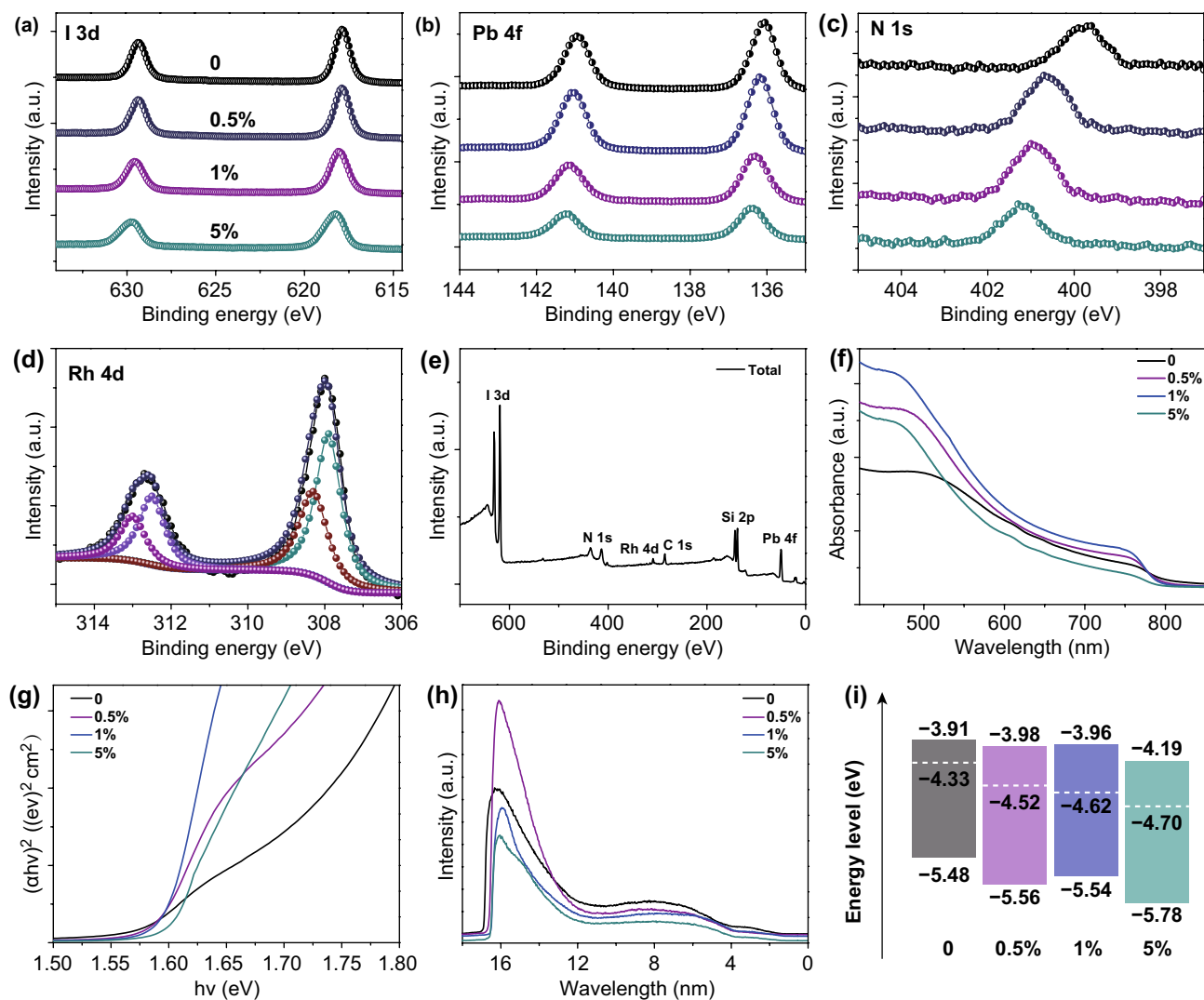
**Fig. 3** XPS of **a** I 3*d*, **b** Pb 4*f*, **c** N 1*s* from MAPbI$_3$:*x*Rh (where *x*=0, 0.5%, 1% and 5%). **d** Rh 4*d* from MAPbI$_3$:*x*Rh (where *x*=1%). **e** XPS of total elements from the MAPbI$_3$:*x*Rh (where *x*=1%). **f** Absorbance coefficient of MAPbI$_3$:*x*Rh. **g** Estimated bandgap potential of perovskite films. **h** UPS of MAPbI$_3$:*x*Rh (where *x*=0, 0.5%, 1% and 5%). **i** Energy level diagram of MAPbI$_3$:*x*Rh (where *x*=0, 0.5%, 1% and 5%)

1.09 V, fill factor (FF) of 0.78, PCE of 19.09%. The PSCs prepared by MAPbI$_3$:*x*Rh (where *x*=1%) possess high PCE of 20.71% (Table 1), which is increased approximately 10% compared to that of based on MAPbI$_3$. However, the properties of PSCs based on MAPbI$_3$:*x*Rh (where *x*=5%) have decreased. The MAPbI$_3$:*x*Rh (where *x*=5%) films possess poor-quality films, which leads to large leakage current, low $J_{sc}$. To ensure repeatability of device performance, over 40 PSCs are fabricated and characterized (Tables S5–S8). PSCs based on MAPbI$_3$ show a wide photoresponse in the range of 350-800 nm, and external quantum efficiency (EQE) values were close to 85%. EQE values of devices fabricated

by 1% Rh incorporation are risen to more than 90%. The photocurrent of 21.62, 22.13, 23.37 and 21.00 mA cm$^{-2}$ is obtained by integration of EQE spectrum in the range of 350–800 nm, which is similar to the $J_{sc}$ from the results of *J–V* measurement.

Charge transfer characteristics of PSCs were studied by electrochemical impedance spectroscopy (EIS). The EIS was tested in the dark under applied bias of $V_{OC}$. Under such a condition, the charge carrier recombination resistance ($R_{REC}$) attained the lowest value ($R_{REC} \ll R_{CT}$), and $R_{CT}$ is the charge transfer resistance. Semicircle from EIS measurement is formed by series resistor ($R_s$), charge transport
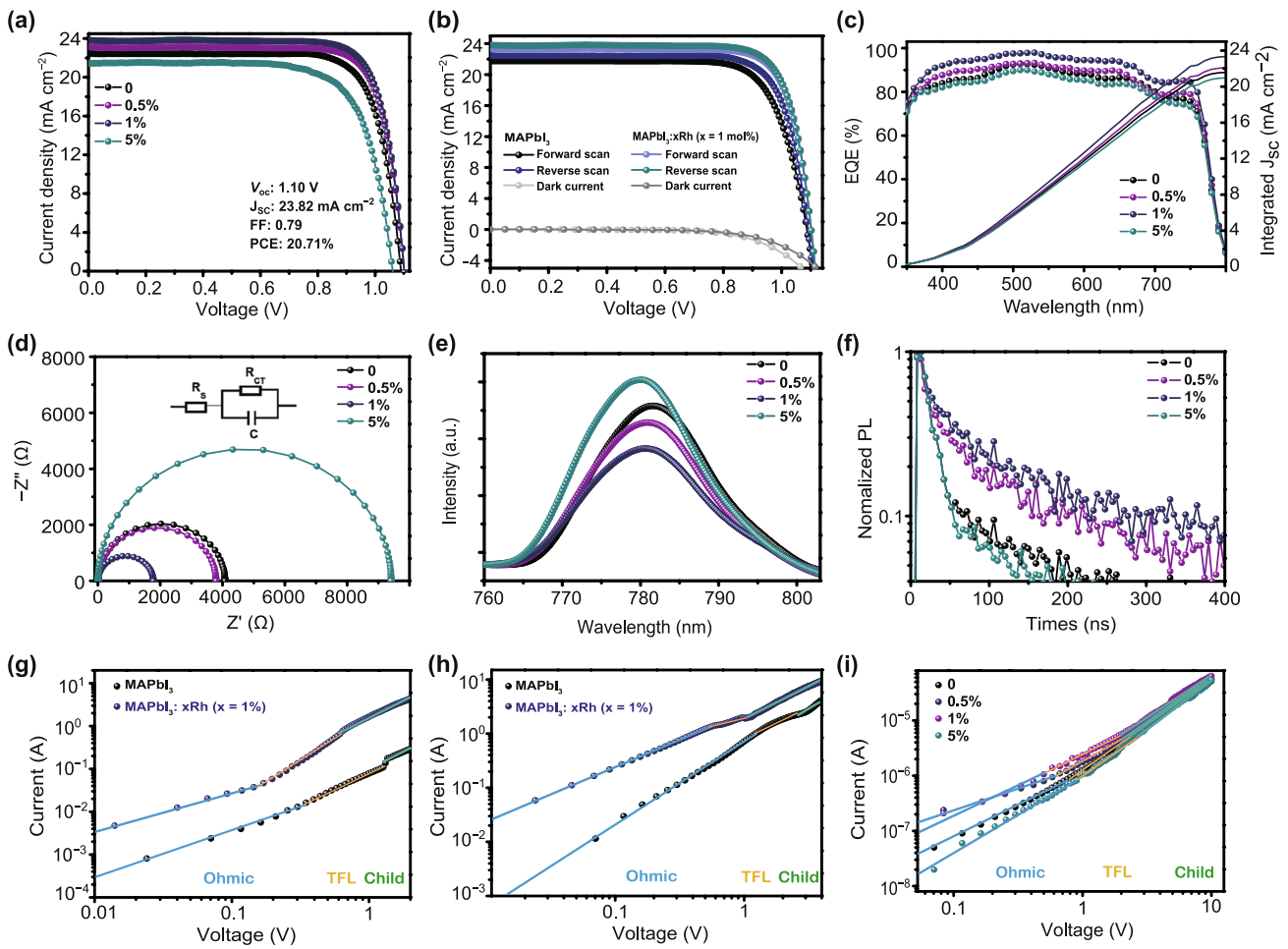
**Fig. 4** **a** *J–V*, **c** EQE data and **d** Nyquist plots of PSCs fabricated by MAPbI$_3$:*x*Rh (where *x* = 0, 0.5%, 1% and 5%). **b** Forward and reverse direction *J–V* of PSC fabricated by MAPbI$_3$:*x*Rh (where *x* = 0, 1%). **e** PL spectra of the MAPbI$_3$:*x*Rh/SnO$_2$ films. **f** Time-resolved PL spectrum of perovskite films based on MAPbI$_3$:*x*Rh (where *x* = 0, 0.5%, 1% and 5%). *I–V* characteristic of **g** hole-only device, **h** electron-only device prepared by MAPbI$_3$ and MAPbI$_3$:*x*Rh (*x* = 1%). **i** Perovskite-only device fabricated by MAPbI$_3$:*x*Rh (where *x* = 0, 0.5%, 1% and 5%)

**Table 1** Device photovoltaic parameters of devices based on MAPbI$_3$:*x*Rh (where *x* = 0, 0.5%, 1% and 5%)

| Devices | | $V_{oc}$ (V) | $J_{sc}$ (mA cm$^{-2}$) | FF | PCE (%) |
|---|---|---|---|---|---|
| MAPbI$_3$ | Best | 1.09 | 22.46 | 0.78 | 19.09 |
| | Average | 1.07 ± 0.02 | 22.60 ± 0.8 | 0.75 ± 0.04 | 18.19 ± 0.96 |
| 0.5% Rh | Best | 1.09 | 23.13 | 0.79 | 20.01 |
| | Average | 1.08 ± 0.02 | 22.72 ± 0.43 | 0.78 ± 0.03 | 19.37 ± 1.02 |
| 1% Rh | Best | 1.10 | 23.82 | 0.79 | 20.71 |
| | Average | 1.10 ± 0.03 | 23.47 ± 0.41 | 0.76 ± 0.05 | 19.56 ± 1.01 |
| 5% Rh | Best | 1.06 | 21.44 | 0.73 | 16.76 |
| | Average | 1.03 ± 0.03 | 21.30 ± 1.06 | 0.67 ± 0.06 | 14.98 ± 1.78 |

resistor ($R_{ct}$) and capacitor (CPE1). The inset of Fig. 4d is equivalent circuit diagram [41]. Because all devices have the same structure, $R_S$ values are basically the same (Fig.

S6). The radius of the arc represents the value level of $R_{ct}$. The lowest $R_{ct}$ of MAPbI$_3$:*x*Rh (*x* = 1%) reveals that a tiny amount of Rh-incorporated can enhance charge transport

capacity. Therefore, supreme $J_{sc}$ is obtained from PSCs based on MAPbI$_3$:$x$Rh ($x$ = 1%). Figure 4e presents steady-state photoluminescence (PL) spectrum of MAPbI$_3$:$x$Rh/ SnO$_2$ films. Excitation wavelength is 465 nm. For MAPbI$_3$ films, a peak was around 780 nm. With the increase of Rh-incorporated content, the PL peak to appear slight blue shift. From Fig. 4e, the lower intensity of MAPbI$_3$:$x$Rh (where $x$ = 0.5%, 1%) film indicated extract electron carriers more effectively to SnO$_2$ electron transport layer, which is consistent with the larger FF.

The device measured in the forward and reverse scanning directions. Hysteresis characteristics of photocurrent are analyzed by the results of $J$–$V$ curves. Photocurrent hysteresis can be expressed by photocurrent hysteresis index (HI). The formula is (Eq. 1) [28]:

$$HI = \frac{PCE_{reverse} - PCE_{forward}}{PCE_{reverse}} \tag{1}$$

The HI of PSCs fabricated by MAPbI$_3$:$x$Rh ($x$ = 0, 1%) is 0.042 and 0.020. Previous reports have shown that photocurrent hysteresis of devices mainly came from trap-induced carrier prevention. Therefore, lower photocurrent hysteresis indexes of devices fabricated by MAPbI$_3$:$x$Rh ($x$ = 1%) suggest that higher trap-induced carrier prevention is taken.

The time-resolved PL spectrums of MAPbI$_3$:$x$Rh films are shown in Fig. 4f. Usually, $\tau_1$ is attributed to bimolecular recombination of photogenerated carriers, while $\tau_2$ is due to trap-assisted recombination. Table S4 shows the details of parameters of carrier lifetimes. The decay time of pristine perovskite is $\tau_1$ = 67 ns and $\tau_2$ = 693 ns. The decay time of MAPbI$_3$:$x$Rh ($x$ = 1%) is $\tau_1$ = 63 ns and $\tau_2$ = 818 ns. The passivation of rhodium ion mainly reduces grain boundaries and defects and increases carrier lifetime. To find the difference in average carrier lifetime ($\tau_{avg}$), the formula was defined as follows (Eq. 2) [42]:

$$\tau_{avg} = \frac{\Sigma A_i \tau_i^2}{\Sigma A_i \tau_i} \tag{2}$$

The $\tau_{avg}$ of pristine MAPbI$_3$ film is only 671 ns. MAPbI$_3$:$x$Rh (where $x$ = 0.5%, 1%) films possess longer $\tau_{avg}$, which is 726 and 796 ns. Because there is no charge transport layer, non-radiative recombination is the main reason for decay lifetime. Rh$^{3+}$ incorporation has long lifetime, which is reduced recombination and improve photocurrent of PSCs.

Space charge limited current (SCLC) was measured to study the mobility and defects density of perovskite films. Figure S7 shows device structures of the hole-only diode and

the electron-only diode are shown. For electron-only device, SnO$_2$ and PCBM layer are used as the electron transport (blocking holes) layer being coated on both sides of the perovskite. For the hole-only device, the NiO and Spiro-MeO-TAD layer is utilized as hole transport (blocking electrons) layer being coated on both sides of the perovskite. The current versus voltage ($I$–$V$) was tested under dark conditions by a Keithley model 2400. Three regions were evident in the experimental data. $I$–$V$ characteristics show three different regions: a linear ohmic region at low voltage (represented by the blue line); a trap-filling region from mediate voltage to the trap-filled limit voltage ($V_{TFL}$) (represented by the orange line); a Child's region (represented by the green line). The formula for trap density is [28]:

$$n_t = \frac{2\varepsilon\varepsilon_0 V_{TFL}}{eL^2} \tag{3}$$

(where $V$ is the relative dielectric constant of perovskite hybrid materials, $\varepsilon_0$ is vacuum permittivity, $L$ is the thickness of perovskite layer). The charge carrier mobility ($\mu$) is estimated at the quadratic dependence region. The Mott–Gurney's law is (Eq. 4) [28]:

$$I_d = \frac{9\varepsilon\varepsilon_0 \mu V^2}{8L^3} \tag{4}$$

(where $I_d$ is dark current density, and $V$ is the applied voltage). The trap-filling process for the hole-only device set is at $V_{TFL}$ = 0.33 V for MAPbI$_3$ and $V_{TFL}$ = 0.14 V for MAPbI$_3$:$x$Rh (where $x$ = 1%); the trap-filling process for the electron-only device set is at $V_{TFL}$ = 1.12 V for MAPbI$_3$ and $V_{TFL}$ = 0.57 V for MAPbI$_3$:$x$Rh (where $x$ = 1%). As shown in Table S10, the hole trap density of 1% Rh$^{3+}$-incorporated is $3.10 \times 10^{15}$ cm$^{-3}$ lower than MAPbI$_3$ ($8.09 \times 10^{15}$ cm$^{-3}$). The hole mobility of MAPbI$_3$:$x$Rh (where $x$ = 0, 1%) is $1.29 \times 10^{-3}$ and $2.51 \times 10^{-2}$ cm$^2$ V$^{-1}$ s$^{-1}$. Similarly, the electron trap density of 1% Rh$^{3+}$-incorporated is $1.26 \times 10^{15}$ cm$^{-3}$ smaller than MAPbI$_3$ ($2.74 \times 10^{16}$ cm$^{-3}$). The electron mobility of MAPbI$_3$:$x$Rh (where $x$ = 0, 1%) is $5.38 \times 10^{-3}$ and $1.26 \times 10^{-2}$ cm$^2$ V$^{-1}$ s$^{-1}$. The decrease of trap densities of MAPbI$_3$:$x$Rh (where $x$ = 1%) leads to both electron and hole mobility increase. We also measured $I$–$V$ curves of perovskite-only device by MAPbI$_3$:$x$Rh (where $x$ = 0, 0.5%, 1% and 5%). Because the trap density is proportional to $V_{TFL}$, the trap density of MAPbI$_3$:$x$Rh (where $x$ = 1%) is minimum (Fig. 4i). In polycrystalline perovskite films, there are many defects such as vacancies, dislocations and bond deformation because of the confusion of atomic arrangement on grain boundaries. Defects are mainly distributed on the gain boundaries [43]. The results of defect
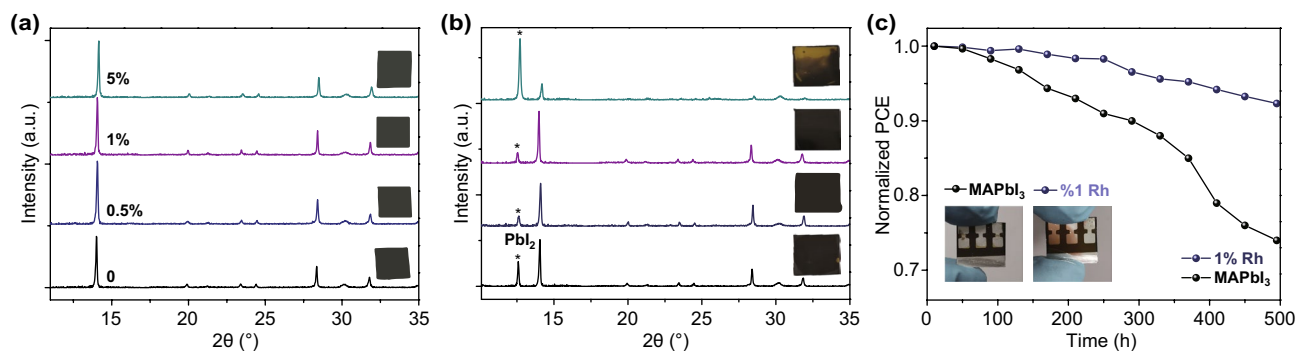
**Fig. 5** **a**, **b** XRD of perovskite films based on $MAPbI_3$ and 1% $Rh^{3+}$-incorporated is exposed in the air before and after two months. **c** PCE changes of perovskite solar cells located in dry air without encapsulation for 500 h

density show that rhodium ion incorporation mainly plays the role of passivation grain boundary.

XRD patterns of $MAPbI_3$ and 1% Rh-incorporated perovskite films are exposed in the humid air before and after two months (Fig. 5). The aging rate of perovskite films is related to $PbI_2$ separated. Peak value of $PbI_2$ is higher, and perovskite film aging is faster. From Fig. 5b, the perovskite films based on $MAPbI_3$:$x$Rh (where $x = 0.5\%$ and 1%) aged slower than that based on $MAPbI_3$ films. The addition of $Rh^{3+}$ made the perovskite structure more stable once again. The perovskite film stability directly affects the PSCs stability. The PSCs were stored in dry atmosphere without encapsulation for 500 h (Fig. 5c). Figure 5c shows that PSCs based on $MAPbI_3$:$x$Rh (where $x = 1\%$) possess higher stability than that of $MAPbI_3$, maintained 92% of initial PCE after 500 h. Detail performance of PSCs is fabricated by $MAPbI_3$ and $MAPbI_3$:$x$Rh with different aged time at dry air (Fig. S11 and Table S12).

## 4  Conclusion

Herein, $Rh^{3+}$ incorporation with tiny amount can help nucleation of perovskite grain, passivate grain boundary defects and improve properties of PSCs. In addition, $Rh^{3+}$ incorporation with perovskite can contribute to preparing larger crystalline and uniform film, reducing trap-state density and enlarging charge carrier lifetime. Therefore, planar heterojunction PSCs by $MAPbI_3$:$x$Rh$^{3+}$ perovskite materials possess PCE of 20.71% without obvious photocurrent hysteresis. Meanwhile, the devices of $Rh^{3+}$-incorporated have high stability within 500 h without

encapsulation in dry air. This work highlights the advantages of $Rh^{3+}$ incorporation in the capabilities of PSCs, which will promote the future industrial application.

## References

1. B. Shi, L. Duan, Y. Zhao, J. Luo, X. Zhang, Semitransparent perovskite solar cells: from materials and devices to

applications. Adv. Mater. **32**(3), 1806474 (2019). https://doi.org/10.1002/adma.201806474

2. K.T. Cho, G. Grancini, Y. Lee, E. Oveisi, J. Ryu et al., Selective growth of layered perovskites for stable and efficient photovoltaics. Energy Environ. Sci. **11**(4), 952–959 (2018). https://doi.org/10.1039/C7EE03513F

3. Y. Liu, Z. Yang, D. Cui, X. Ren, J. Sun et al., Two-inch-sized perovskite $CH_3NH_3PbX_3$ (X = Cl, Br, I) crystals: growth and characterization. Adv. Mater. **27**(35), 5176–5183 (2015). https://doi.org/10.1002/adma.201502597

4. Q. Jiang, Y. Zhao, X. Zhang, X. Yang, Y. Chen et al., Surface passivation of perovskite film for efficient solar cells. Nat. Photonics **13**(7), 460–466 (2019). https://doi.org/10.1038/s41566-019-0398-2

5. W. Liu, L. Chu, R. Hu, R. Zhang, Y. Ma et al., Diameter engineering on $TiO_2$ nanorod arrays for improved hole-conductor-free perovskite solar cells. Sol. Energy **166**, 42–49 (2018). https://doi.org/10.1016/j.solener.2018.03.037

6. S. Ghosh, T. Singh, Role of ionic liquids in organic–inorganic metal halide perovskite solar cells efficiency and stability. Nano Energy **63**, 103828 (2019). https://doi.org/10.1016/j.nanoen.2019.06.024

7. C. Chen, Z. Song, C. Xiao, D. Zhao, N. Shrestha et al., Achieving a high open-circuit voltage in inverted wide-bandgap perovskite solar cells with a graded perovskite homojunction. Nano Energy **61**, 141–147 (2019). https://doi.org/10.1016/j.nanoen.2019.04.069

8. L. Chu, J. Zhang, W. Liu, R. Zhang, J. Yang et al., A facile and green approach to synthesize mesoporous anatase $TiO_2$ nanomaterials for efficient dye-sensitized and hole-conductor-free perovskite solar cells. ACS Sustain. Chem. Eng. **6**(4), 5588–5597 (2018). https://doi.org/10.1021/acssuschemeng.8b00607

9. L. Chu, W. Ahmad, W. Liu, J. Yang, R. Zhang et al., Lead-free halide double perovskite materials: a new superstar toward green and stable optoelectronic applications. Nano-Micro Lett. **11**(1), 16 (2019). https://doi.org/10.1007/s40820-019-0244-6

10. E. Mosconi, B. Merabet, D. Meggiolaro, A. Zaoui, F. De Angelis, First-principles modeling of bismuth doping in the $MAPbI_3$ perovskite. J. Phys. Chem. C **122**(25), 14107–14112 (2018). https://doi.org/10.1021/acs.jpcc.8b01307

11. L.Q. Xie, L. Chen, Z.A. Nan, H.X. Lin, T. Wang et al., Understanding the cubic phase stabilization and crystallization kinetics in mixed cations and halides perovskite single crystals. J. Am. Chem. Soc. **139**(9), 3320–3323 (2017). https://doi.org/10.1021/jacs.6b12432

12. W. Liu, L. Chu, N. Liu, Y. Cheng, F. Wu et al., Simultaneously enhanced efficiency and stability of perovskite solar cells with $TiO_2$@CdS core–shell nanorods electron transport layer. Adv. Mater. Interfaces **6**(5), 1801976 (2019). https://doi.org/10.1002/admi.201801976

13. Y. Huang, L. Li, Z. Liu, H. Jiao, Y. He et al., The intrinsic properties of $FA_{(1-x)}MAxPbI_3$ perovskite single crystals. J. Mater. Chem. A **5**(18), 8537–8544 (2017). https://doi.org/10.1039/C7TA01441D

14. J.S. Manser, P.V. Kamat, Band filling with free charge carriers in organometal halide perovskites. Nat. Photonics **8**(9), 737–743 (2014). https://doi.org/10.1038/nphoton.2014.171

15. National renewable energy laboratory, Best research-cell efficiencies. www.nrel.gov/pv/assets/pdfs/best-research-cell-efficiencies.20190802.pdf

16. J. Zhang, Q. Wang, L. Wang, X.A. Li, W. Huang, Layer-controllable $WS_2$-reduced graphene oxide hybrid nanosheets with high electrocatalytic activity for hydrogen evolution. Nanoscale **7**(23), 10391–10397 (2015). https://doi.org/10.1039/C5NR01896J

17. Y.C. Kim, N.J. Jeon, J.H. Noh, W.S. Yang, J. Seo et al., Beneficial effects of $PbI_2$ incorporated in organo-lead halide perovskite solar cells. Adv. Energy Mater. **6**(4), 1502104 (2016). https://doi.org/10.1002/aenm.201502104

18. W. Zhao, Z. Yao, F. Yu, D. Yang, S.F. Liu, Alkali metal doping for improved $CH_3NH_3PbI_3$ perovskite solar cells. Adv. Sci. **5**(2), 1700131 (2018). https://doi.org/10.1002/advs.201700131

19. Y. Zhang, C.C. Zhang, C.H. Gao, M. Li, X.J. Ma et al., N-type doping of organic–inorganic hybrid perovskites toward high-performance photovoltaic devices. Sol. RRL **3**(2), 1800269 (2019). https://doi.org/10.1002/solr.201800269

20. J. Zhang, R. Chen, Y. Wu, M. Shang, Z. Zeng, Y. Zhang, Y. Zhu, L. Han, Extrinsic movable ions in $MAPbI_3$ modulate energy band alignment in perovskite solar cells. Adv. Energy Mater. **8**(5), 1701981 (2018). https://doi.org/10.1002/aenm.201701981

21. W. Liu, L. Chu, N. Liu, Y. Ma, R. Hu et al., Efficient perovskite solar cells fabricated by manganese cations incorporated in hybrid perovskites. J. Mater. Chem. C **7**(38), 11943–11952 (2019). https://doi.org/10.1039/C9TC03375K

22. Z. Shi, Z. Guo, Y. Chen, Q. Li, Y. Pan, H. Zhang, Y. Xia, W. Huang, Lead-free organic–inorganic hybrid perovskites for photovoltaic applications: recent advances and perspectives. Adv. Mater. **29**(16), 1605005 (2017). https://doi.org/10.1002/adma.201605005

23. W. Xu, L. Zheng, X. Zhang, Y. Cao, T. Meng et al., Efficient perovskite solar cells fabricated by Co partially substituted hybrid perovskite. Adv. Energy Mater. **8**(14), 1703178 (2018). https://doi.org/10.1002/aenm.201703178

24. X. Gong, L. Guan, H. Pan, Q. Sun, X. Zhao et al., Highly efficient perovskite solar cells via nickel passivation. Adv. Funct. Mater. **28**(50), 1804286 (2018). https://doi.org/10.1002/adfm.201804286

25. M.T. Klug, A. Osherov, A.A. Haghighirad, S.D. Stranks, P.R. Brown et al., Tailoring metal halide perovskites through metal substitution: influence on photovoltaic and material properties. Energy Environ. Sci. **10**(1), 236–246 (2017). https://doi.org/10.1039/C6EE03201J

26. Z. Xiao, Z. Song, Y. Yan, From lead halide perovskites to lead-free metal halide perovskites and perovskite derivatives. Adv. Mater. **31**(47), e1803792 (2019). https://doi.org/10.1002/adma.201803792

27. J. Lu, S. Chen, Q. Zheng, Defect passivation of $CsPbI_2Br$ perovskites through Zn(II) doping: toward efficient and stable

solar cells. Sci. China Chem. **62**, 1044–1050 (2019). https://doi.org/10.1007/s11426-019-9486-0

28. K. Wang, L. Zheng, T. Zhu, X. Yao, C. Yi et al., Efficient perovskite solar cells by hybrid perovskites incorporated with heterovalent neodymium cations. Nano Energy **61**, 352–360 (2019). https://doi.org/10.1016/j.nanoen.2019.04.073

29. Z.K. Wang, M. Li, Y.G. Yang, Y. Hu, H. Ma et al., High efficiency Pb–In binary metal perovskite solar cells. Adv. Mater. **28**(31), 6695–6703 (2016). https://doi.org/10.1002/adma.201600626

30. J.W. Wang, Z. Wang, S. Pathak, W. Zhang, D.W. de Quilettes et al., Efficient perovskite solar cells by metal ion doping. Energy Environ. Sci. **9**(9), 2892–2901 (2016). https://doi.org/10.1039/C6EE01969B

31. L. Wang, H. Zhou, J. Hu, B. Huang, M. Sun et al., A $Eu^{3+}$–$Eu^{2+}$ ion redox shuttle imparts operational durability to Pb–I perovskite solar cells. Science **363**(6424), 265–270 (2019). https://doi.org/10.1126/science.aau5701

32. K. Maeda, Rhodium-doped barium titanate perovskite as a stable p-type semiconductor photocatalyst for hydrogen evolution under visible light. ACS Appl. Mater. Interfaces **6**(3), 2167–2173 (2014). https://doi.org/10.1021/am405293e

33. K. Iwashina, A. Kudo, Rh-doped $SrTiO_3$ photocatalyst electrode showing cathodic photocurrent for water splitting under visible-light irradiation. J. Am. Chem. Soc. **133**(34), 13272–13275 (2011). https://doi.org/10.1021/ja2050315

34. N. Li, S. Tao, Y. Chen, X. Niu, C.K. Onwudinanti et al., Cation and anion immobilization through chemical bonding enhancement with fluorides for stable halide perovskite solar cells. Nat. Energy **4**(5), 408–415 (2019). https://doi.org/10.1038/s41560-019-0382-6

35. L. Wei, W. Ma, C. Lian, S. Meng, Benign interfacial iodine vacancies in perovskite solar cells. J. Phys. Chem. C **121**(11), 5905–5913 (2017). https://doi.org/10.1021/acs.jpcc.6b12583

36. X. Niu, Y. Li, Y. Zhang, Z. Zhou, J. Wang, Greatly enhanced photoabsorption and photothermal conversion of antimonene quantum dots through spontaneously partial oxidation. ACS Appl. Mater. Interfaces **11**(19), 17987–17993 (2019). https://doi.org/10.1021/acsami.9b02771

37. X. Niu, X. Bai, Z. Zhou, J. Wang, Rational design and characterization of direct Z-scheme photocatalyst for overall water splitting from excited state dynamics simulations. ACS Catal. **10**, 1976–1983 (2020). https://doi.org/10.1021/acscatal.9b04753

38. L. Zhou, J. Su, Z. Lin, D. Chen, W. Zhu et al., Theoretical and experimental investigation of mixed Pb–In halide perovskites. J. Phys. Chem. C **122**(28), 15945–15953 (2018). https://doi.org/10.1021/acs.jpcc.8b05267

39. D. Bai, J. Zhang, Z. Jin, H. Bian, K. Wang et al., Interstitial $Mn^{2+}$-driven high-aspect-ratio grain growth for low-trap-density microcrystalline films for record efficiency $CsPbI_2Br$ solar cells. ACS Energy Lett. **3**(4), 970–978 (2018). https://doi.org/10.1021/acsenergylett.8b00270

40. Y. Zhao, P. Zhu, M. Wang, S. Huang, Z. Zhao et al., A polymerization-assisted grain growth strategy for efficient and stable perovskite solar cells. Adv. Mater. (2020). https://doi.org/10.1002/adma.201907769

41. H. Sun, J. Zhang, X. Gan, L. Yu, H. Yuan et al., Pb-reduced $CsPb_{0.9}Zn_{0.1}I_2Br$ thin films for efficient perovskite solar cells. Adv. Energy Mater. **9**(25), 1900896 (2019). https://doi.org/10.1002/aenm.201900896

42. Y. Ma, H. Zhang, Y. Zhang, R. Hu, M. Jiang et al., Enhancing the performance of inverted perovskite solar cells via grain boundary passivation with carbon quantum dots. ACS Appl. Mater. Interfaces **11**(3), 3044–3052 (2018). https://doi.org/10.1021/acsami.8b18867

43. Z. Ni, C. Bao, Y. Liu, W. Wu, S. Chen, Q. Jiang et al., Resolving spatial and energetic distributions of trap states in metal halide perovskite solar cells. Science **367**(6484), 1352–1358 (2020). https://doi.org/10.1126/science.aba0893